THE JOURNAL OF PHYSICAL CHEMISTRY C

Article

pubs.acs.org/JPCC

Initial-Stage Oxidation of $Ni_3Al(100)$ and -(110) from Ab Initio Thermodynamics

Likun Wang,[†] Canying Cai,[†] Yichun Zhou,*[,†,‡] and Guangwen Zhou*[,§]

[†]Hunan Provincial Key laboratory of Thin Film Materials and Devices, School of Materials Science and Engineering, Xiangtan University, Hunan 411105, China

[‡]Key Laboratory of Key Film Materials & Application for Equipment of Hunan Province, Xiangtan University, Hunan 411105, China

[§]Department of Mechanical Engineering & Materials Science and Engineering Program, State University of New York at Binghamton, Binghamton, New York 13902, United States

ABSTRACT: The microscopic mechanisms of the initial-stage oxidation of the $Ni_3Al(100)$ and $Ni_3Al(110)$ surfaces are comparatively studied using ab initio calculations based on density-functional theory and thermodynamics considerations. The surface energies of the two surfaces as functions of aluminum and oxygen chemical potentials are constructed and show that the formation of any antisite defects is not favorable at the $Ni_3Al(100)$ surface, whereas Al antisite defects are favorable at the $Ni_3Al(110)$ surface. The surface phase diagrams of the $Ni_3Al(100)$ and -(110) surfaces with different antisite defects and at the various oxygen coverages are determined. These results show that oxygen adsorption enhances Al surface segregation at the initial stage of oxidation for both surfaces and that the $Ni_3Al(100)$ surface is thermodynamically more favored to oxidize completely at a lower oxygen coverage than the $Ni_3Al(110)$ surface.

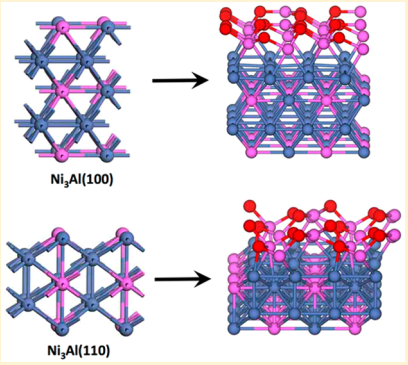

1. INTRODUCTION

Ni-based superalloys are a class of technologically important intermetallic materials that process a high melting point, low density, good oxidation and corrosion resistance, and metal-like electrical and thermal conductivities.[1,2] The unique combination of these properties makes the Ni-based alloys the material of choice for high-temperature applications, including chemical processing, power generation, and aerospace propulsion. For instance, the volume fraction of the Ni_3Al is around 70% for the blades and vanes of modern gas turbines as the precipitation strengthener and antioxidation phase in superalloys. However, the surfaces of all Ni-base alloys show strong chemical reactivity toward oxygen, and their practical applications at elevated temperatures are still hindered by the competitive oxidation of Al and Ni that can prevent the formation of a dense and protective α-Al_2O_3 layer.[3] The growth of a protective aluminum oxide layer depends on the local reactivities of the alloy, which depend on a number of convoluted factors, including temperature, oxygen pressure, surface structure, and composition.

As a prototype of multicomponent surfaces, NiAl(100) and -(110) have been studied extensively,[4−9] both experimentally and theoretically, to understand the atomistic mechanism of the surface-oxidation-induced Al_2O_3 formation. Recently, the aluminum oxide film growth on NiAl(100) has been shown to proceed via the surface diffusion of Al atoms detached from substrate steps,[4] whereas the Al_2O_3 growth on NiAl(110) involves the participation of Al atoms supplied from the bulk,[5,6] demonstrating the strong dependence of the oxidation mechanism on the surface structure and crystallography orientation. On the theoretical side, density-functional theory (DFT) calculations have been employed to study oxygen adsorption at the NiAl(100)[4] and NiAl(110)[7,8] surfaces and the reaction barriers of the initial stages of oxidation based on the electronic structure, atomic geometry, and energetic properties. Furthermore, Liu et al. reported their ab initio thermodynamics calculations for the oxidation mechanism of the intermetallic Ti_3Al compound, a relevant high-temperature alloy system.[10]

By contrast, the theoretical study on the similarly important system of the intermetallic Ni_3Al compound is much less with regard to its atomic-scale oxidation mechanism. Compared to the NiAl alloy, the Ni_3Al may be less oxidation resistant because it contains less Al and thus has a larger tendency to form less protective multiple oxides (e.g., Al_2O_3, NiO) that involve the redistribution and segregation of Ni and Al atoms in the substrate. While the classical Wagner's oxidation theory[11] provides a general description of the oxidation behavior of binary alloys from a macroscopic point of view that stipulates the correlation of the oxide formation with alloy composition and activities of the metal and oxygen, the microscopic process initiating the selective oxidation of one component, commonly observed in most metal alloys exposed to an oxidizing environment, still remains elusive. In the present work, we report a comparative study of DFT and the first-principles thermodynamics investigations of adsorption of oxygen atoms at the $Ni_3Al(100)$ and -(110) surfaces. Our aims are to find

Received: May 15, 2017
Revised: August 14, 2017
Published: August 18, 2017

DOI: 10.1021/acs.jpcc.7b04674
J. Phys. Chem. C 2017, 121, 19191−19200

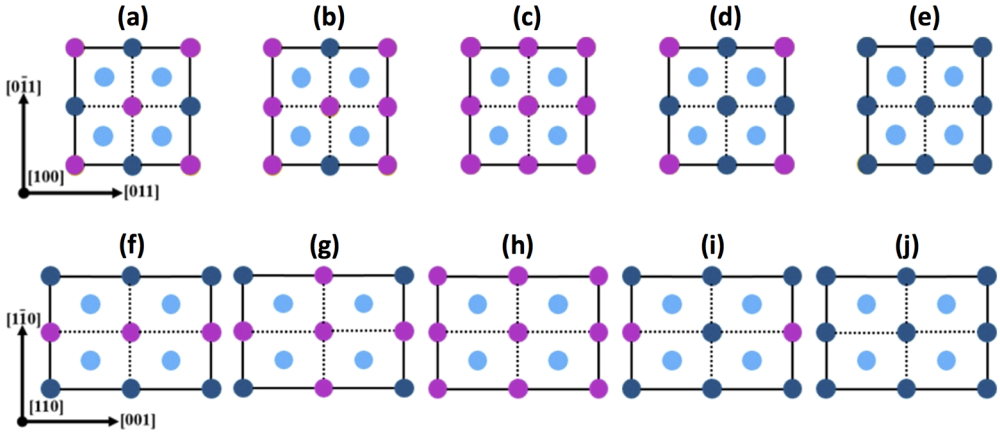

Figure 1. Schematic top view of the $Ni_3Al(100)$ and -(110) surfaces with possible antisite defects for five cases: (a, f) the perfect surface, (b, g) the surface with one Al antisite defect [denoted by $Ni_3Al(100)$-1Al, $Ni_3Al(110)$-1Al], (c, h) the surface with two Al antisite defects [denoted by $Ni_3Al(100)$-2Al, $Ni_3Al(110)$-2Al], (d, i) the surface with one Ni antisite defect [denoted by $Ni_3Al(100)$-1Ni, $Ni_3Al(110)$-1Ni], and (e, j) the surface with two Ni antisite defects [denoted by $Ni_3Al(100)$-2Ni, $Ni_3Al(110)$-2Ni]. Blue and pink spheres represent Ni and Al atoms in the surface layer, respectively. Light blue spheres represent Ni atoms in the second (subsurface) layer.

active surface sites for the adsorption of oxygen and their dependence on the crystallographic orientation for the selective oxidation of Al atoms, as well as to identify the relative stability of the oxygenated surfaces as a function of the chemical potential of Al and O, from which we provide a clear atomistic mechanism for the initial-stage oxidation of the Ni_3Al surfaces.

2. COMPUTATION METHODS

2.1. DFT Calculations. The ab initio calculations are based on DFT[12,13] and performed with the VASP[14−16] code using projector augmented wave (PAW)[17,18] potentials in conjunction with a plane-wave cut-off energy of 500 eV and PW91 generalized gradient approximation (GGA).[19] Electron smearing is carried out following the Methfessel−Paxton technique[20] with order $N = 1$ and width of the smearing $\sigma = 0.2$. Self-consistent solutions are obtained by employing the $(4 \times 4 \times 1)$ Monkhorst−Pack[21] mesh in the Brillouin zone for the (2×2) surface unit cell.

Ni_3Al has an ordered cubic ($L1_2$) structure with the space group $Pm\bar{3}m$. Our calculated bulk lattice constant obtained from the energy minimization of the bulk Ni_3Al unit cell using a Monkhorst−Pack mesh of $(15 \times 15 \times 15)$ is 3.568 Å, which is in good agreement with the experimental value of 3.57 Å[22] and with previous calculations.[23] The $Ni_3Al(100)$ and -(110) surfaces are constructed by cleaving supercells made from the bulk Ni_3Al. Successive slabs with the (2×2) surface unit cell and five atomic layers are separated by a vacuum region of 15 Å. The atoms in the two bottom layers of the slab are fixed, while the top three layers of the slab are allowed to relax until the forces on each of them are less than 0.01 eV/Å. The surface areas of the (2×2) surface unit cell are 25.46 $Å^2$ for the $Ni_3Al(100)$ surface and 36.01 $Å^2$ for the $Ni_3Al(110)$ surface, respectively. This means that the $Ni_3Al(100)$ surface is more closely packed than the $Ni_3Al(110)$ surface. To verify our values, we also relax the $Ni_3Al(100)$ and $Ni_3Al(110)$ slabs and compare the results with the previously reported calculated results.[23,24] The interlayer separation is measured by the percentage of changes in relaxed distances and original distances. For the $Ni_3Al(100)$ slab, our results show that after structural relaxation, the spacing change between the first and second Ni layers is −3.027% and that between the first Al and second Ni layers is −2.130%, which are similar to the previously calculated values of −2.859% and −2.466%,[24] while slightly different from the experimental value of −2.809% for the first and second Ni layers and a larger difference from the experimental value of 1.124% for the first Al and second Ni layers.[25] For the $Ni_3Al(110)$ slab, our results show that after structural relaxation, the spacing change between the first and second Ni layers is −11.261% and brween the first Al and second Ni layers is −9.992%, which are similar to the previously calculated values of −10.595% and −9.618%,[23] with a slight difference from the experimental values of −11.835% and −10.643%.[26] The percentage differences between the calculated and experimental values are probably due to the limited layers involved in the DFT calculations.

2.2. First-Principles Atomistic Thermodynamics Calculations. We employ a first-principles atomistic thermodynamic framework to assess the relative stability of the considered surfaces as a function of the chemical potential of Al and O. The thermodynamic stability of a specified surface depends on its surface energy. The following formulations employed in our calculations are based on other works.[10,27−33] The surface energy (σ) can be calculated as

$$\sigma = \frac{1}{S}(E_{Ni_3Al} - N_{Ni}E_{Ni} - N_{Al}E_{Al} - N_OE_O) \quad (1)$$

where S is the surface area and E_{Ni_3Al} is the total energy of the slab. E_{Ni}, E_{Al}, and E_O denote the chemical potential of Ni, Al, and O, respectively. The number of Ni, Al, and O atoms in the system is denoted by N_{Ni}, N_{Al}, and N_O, respectively.

We define the relative surface energy (σ_r) of the Ni_3Al slab with the presence of antisite defects relative to that of the perfect Ni_3Al slab as

$$\sigma_r = (\sigma_d - \sigma_p)S = E^d_{Ni_3Al} - E^p_{Ni_3Al} - (N^d_{Ni} - N^p_{Ni})E_{Ni} - (N^d_{Al} - N^p_{Al})E_{Al} \quad (2)$$

where σ_p is the surface energy of Ni_3Al slab without any antisite defects [shown in Figure 1a,f and defined as the perfect $Ni_3Al(100)$ and -(110)]. σ_d is the surface energy of Ni_3Al slab with antisite defects but without oxygen atoms (any of the configurations shown in Figure 1b−e,g−j). $E^p_{Ni_3Al}$ and $E^d_{Ni_3Al}$

DOI: 10.1021/acs.jpcc.7b04674
J. Phys. Chem. C 2017, 121, 19191−19200

denote the total energy of the perfect Ni_3Al slab and the configuration with antisite defects; N^p_{Ni} and N^p_{Ai} denote, respectively, the number of Ni and Al atoms in the perfect Ni_3Al slab. N^d_{Ni} and N^d_{Ai} denote, respectively, the numbers of Ni and Al atoms in the Ni_3Al slab with antisite defects.

Figure 2 shows all possible adsorption sites for oxygen atoms on the perfect $Ni_3Al(100)$ and $Ni_3Al(110)$ surfaces: four on-top

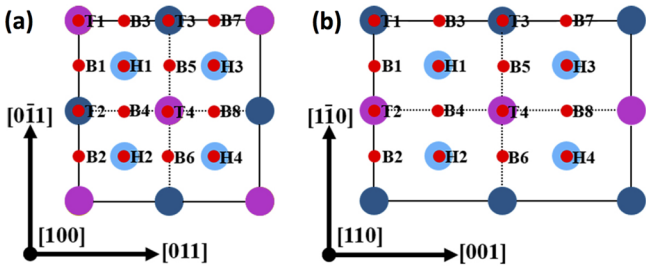

Figure 2. Schematic top view of the possible adsorption sites for O on (a) (100) and (b) (110) surfaces of Ni_3Al. Red spheres represent O atoms in the surface layer. Blue and pink spheres represent Ni and Al atoms in the surface layer, respectively. Light blue spheres represent Ni atoms in the second (subsurface) layer.

(Op) sites, such as the Al on-top and Ni on-top sites (labeled as T1−T4); four 4-fold 2Ni−2Al hollow sites (labeled as H1−H4); and eight bridge sites including Ni−Al short-bridge sites in the $Ni_3Al(100)$ and Ni−Ni and Al−Al long-bridge sites in $Ni_3Al(110)$ (labeled as B1−B8). For the Ni_3Al surfaces with antisite defects shown in Figure 1b−e,g−j, they have the same types of adsorption sites as shown in Figure 2, so it is not necessary to display them here. In this work, the surface configurations with and without antisite defects are investigated sequentially under different oxygen coverages, and the most energetically stable surface configuration from the low oxygen coverage is subsequently used as a starting structure to determine the next stable configuration from the higher oxygen coverage.

The relative stability of the various $O/Ni_3Al(100)$ and $O/Ni_3Al(110)$ surfaces is analyzed by calculating the averaged binding energy per oxygen atom. Here, we define the oxygen coverage θ as the ratio of the number of the oxygen atoms to that of the atoms in the substrate surface layer. The unit of the oxygen coverage is monolayer (ML), and 1 ML is defined as four absorbed oxygen atoms per (2 × 2) surface cell. The averaged oxygen binding energy of the surface as a function of the oxygen coverage θ is calculated as

$$E(\theta) = \frac{1}{N_O}\{E^d_{O/Ni_3Al} - [E^p_{Ni_3Al} + (N^d_{Ni} - N^p_{Ni})E_{Ni} + (N^d_{Al} - N^p_{Al})E_{Al} + N_O E_O]\} \quad (3)$$

where E^d_{O/Ni_3Al} is the total energy of the O-adsorbed Ni_3Al slab. Note that the oxygen binding energy defined by eq 3 includes the change of the surface free energy when a surface antisite defect is involved.

The surface phase diagrams of the $Ni_3Al(100)$ and $Ni_3Al(110)$ surfaces are designed by the surface energy

$$\sigma^O_r = E^d_{O/Ni_3Al} - E^p_{Ni_3Al} - (N^d_{Ni} - N^p_{Ni})E_{Ni} - (N^d_{Al} - N^p_{Al})E_{Al} - N_O E_O \quad (4)$$

Generally, the chemical potential of a specified species is equal at equilibrium in all contact phases, i.e., Ni_3Al alloys and molecular O_2. However, these chemical potentials are not simply the total energies of a certain atom or molecule. In order to avoid the formation of metallic Ni and Al phases, the chemical potentials of Ni and Al must follow $E_{Ni} \le E^{bulk}_{Ni}$ and $E_{Ni} \le E^{bulk}_{Al}$. We particularly suppose that the chemical potential of a specified species in the Ni_3Al surface is equal to that in bulk Ni_3Al; the relation equation follows as $3E_{Ni} + E_{Al} = E^{bulk}_{Ni_3Al}$. Thus, the chemical potential of Al satisfies the constraint $E_{Al} \ge E^{bulk}_{Ni_3Al} - 3E_{Ni}$. The chemical potential of O is allowed to vary with an upper limit determined by the O_2 molecule, which is $E_O \le \frac{1}{2}E_{O_2}$. Combing the results from our ab initio calculations for bulk Ni_3Al, bulk Ni, bulk Al, and molecular O_2, the ranges of the chemical potentials are determined from our calculations to be −5.609 eV < E_{Al} < −3.675 eV and −5.609 eV < E_O < −4.89 eV.

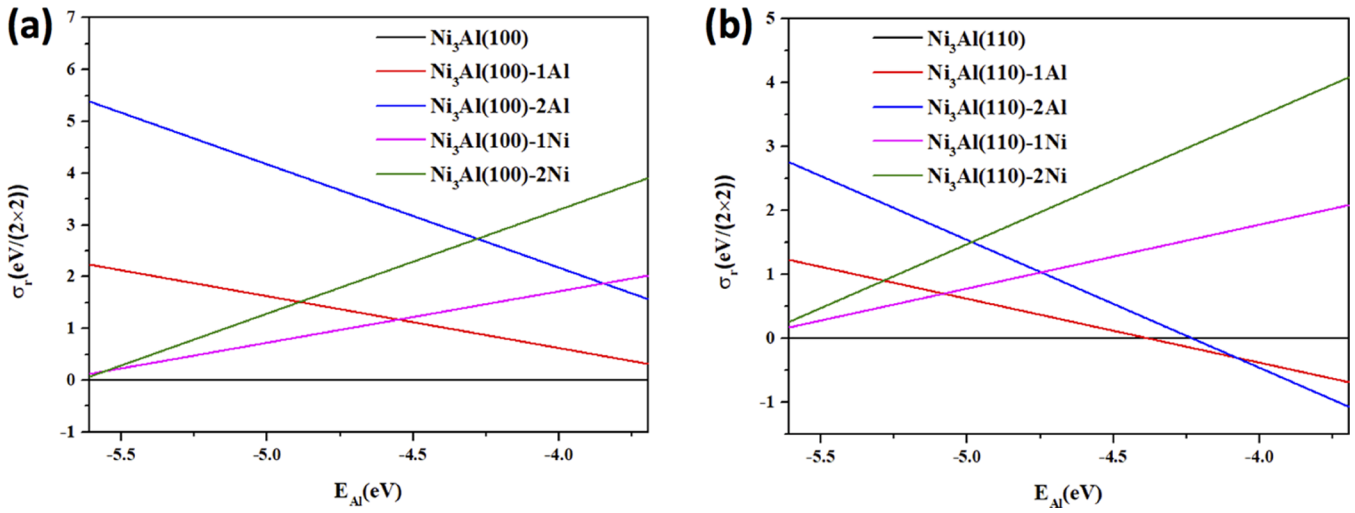

Figure 3. Calculated surface energies of clean $Ni_3Al(100)$ (a) and -(110) (b) with different surface defects as functions of the chemical potential of Al.

DOI: 10.1021/acs.jpcc.7b04674
J. Phys. Chem. C 2017, 121, 19191−19200

3. RESULTS

3.1. Clean Surfaces of $Ni_3Al(100)$ and $Ni_3Al(110)$. We first investigate the relative stability of various atomic configurations of the clean $Ni_3Al(100)$ surfaces (before oxygen adsorption). Here, we consider the cases of the perfect surface without antisite defects [Figure 1a, referred to as $Ni_3Al(100)$] and surfaces with one and two Al antisite defects [Figure 1b,c, denoted $Ni_3Al(100)$-1Al, $Ni_3Al(100)$-2Al] and one or two Ni antisite defects [Figure 1d,e, denoted $Ni_3Al(100)$-1Ni, $Ni_3Al(100)$-2Ni]. It should be noted that the topmost surface layer of either $Ni_3Al(100)$-2Al or $Ni_3Al(100)$-2Ni is composed of all Al atoms or all Ni atoms. The calculated relative surface energies of the perfect surface and four $Ni_3Al(100)$ surfaces with different surface antisite defects (Figure 2a–e) as the functions of E_{Al} are shown in Figure 3a. We can observe that the perfect $Ni_3Al(100)$ surface always has a lower surface energy than other surface configurations with the antisite defects. This fact indicates that the perfect $Ni_3Al(100)$ surface is thermodynamically stable all the time before oxygen adsorption.

We then investigate the relative stability of the various atomic configurations of the clean $Ni_3Al(110)$ surfaces. Here, we consider similarly the cases of the perfect surface without antisite defects [Figure 1f, referred to as $Ni_3Al(110)$] and surfaces with one and two Al antisite defects [Figure 1g,h, denoted $Ni_3Al(110)$-1Al, $Ni_3Al(110)$-2Al] and one or two Ni antisite defects [Figure 1i,j, denoted $Ni_3Al(110)$-1Ni, $Ni_3Al(110)$-2Ni]. The topmost surface layer of either $Ni_3Al(110)$-2Al or $Ni_3Al(110)$-2Ni is composed of all Al atoms or all Ni atoms. The calculated relative surface energies of the perfect $Ni_3Al(110)$ surface and four surfaces with the different surface antisite defects (Figure 1g–j) as the functions of E_{Al} are shown in Figure 3b. We can observe that the $Ni_3Al(110)$-1Ni and $Ni_3Al(110)$-2Ni surfaces always have a higher surface energy than the perfect $Ni_3Al(110)$ surface. This fact indicates that the segregation of Ni atoms to the surface layer is thermodynamically unfavorable. On the other hand, each of the other three surfaces [$Ni_3Al(110)$, $Ni_3Al(110)$-1Al, and $Ni_3Al(110)$-2Al] could represent the most stable configuration in some particular range of the Al chemical potential, which indicates that Al atoms possibly segregate to the surface from the bulk naturally. In particular, the perfect $Ni_3Al(110)$ surface is the lowest over the dominant range of the chemical potential of Al. At the slightly greater Al chemical potential, the $Ni_3Al(110)$ surface with one Al antisite [$Ni_3Al(110)$-1Al] is the most stable, suggesting that Al atoms can segregate to the surface layer of the substrate under the Al-rich condition. Additionally, the surface energy of the $Ni_3Al(110)$-2Al has the lowest energy at very high Al chemical potential, that is, under the extremely Al-rich condition.

3.2. Adsorption of Oxygen. The possible oxygen adsorption sites on the perfect $Ni_3Al(100)$ and -(110) surfaces are shown in Figure 2. The $Ni_3Al(100)$ and -(110) surfaces with antisite defects (as shown in Figure 1) have the same type of surface sites for oxygen adsorption as shown in Figure 2a,b, which are thus not displayed here. The number of calculated possible oxygen adsorption sites is significantly reduced by considering the rotational and mirror symmetries of the system. Figure 4 shows the calculated average oxygen binding energies per oxygen atom as a function of the oxygen coverage for the most stable configuration of oxygen on the perfect $Ni_3Al(100)$, $Ni_3Al(100)$-1Al, $Ni_3Al(100)$-2Al, $Ni_3Al(100)$-1Ni, and $Ni_3Al(100)$-2Ni and the perfect $Ni_3Al(110)$, $Ni_3Al(110)$-1Al, $Ni_3Al(110)$-2Al, $Ni_3Al(110)$-1Ni, and $Ni_3Al(110)$-2Ni. The binding energies for the oxygen with the different Ni antisite defects at the top layer of the $Ni_3Al(100)$ and $Ni_3Al(110)$ surfaces are always higher than that of the perfect Ni_3Al surfaces and the Ni_3Al surfaces with Al antisite defects, which means that the $Ni_3Al(100)$ and $Ni_3Al(110)$ surfaces with the different Ni antisite defects are unstable in the process of oxidation.

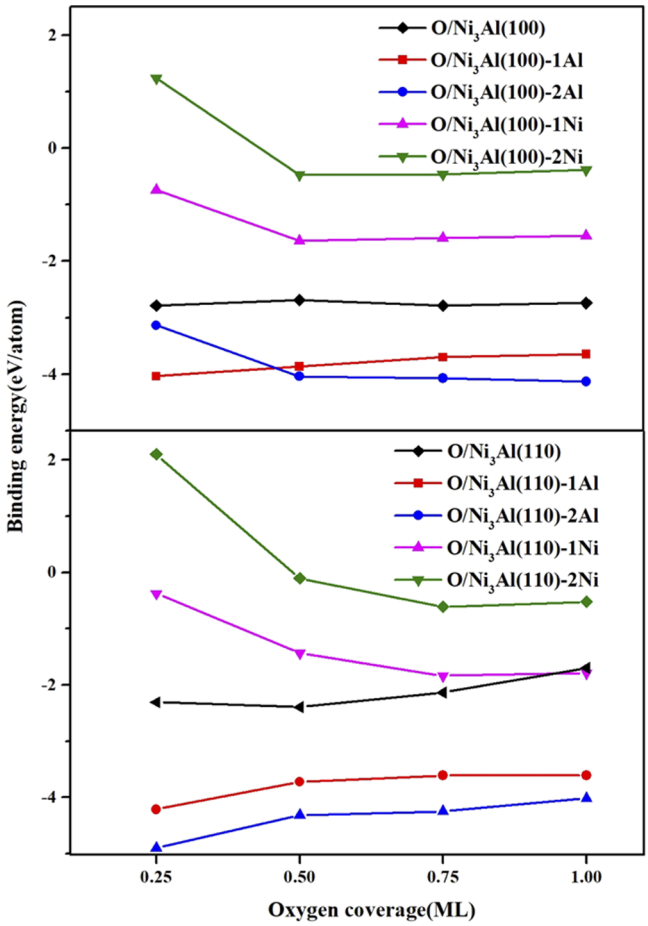

Figure 4. Calculated binding energy per oxygen atom at the most stable adsorption site as a function of the oxygen coverage for the O/$Ni_3Al(100)$, O/$Ni_3Al(100)$-1Al, O/$Ni_3Al(100)$-2Al, O/$Ni_3Al(100)$-1Ni, and O/$Ni_3Al(100)$-2Ni and O/$Ni_3Al(110)$, O/$Ni_3Al(110)$-1Al, O/$Ni_3Al(110)$-2Al, O/$Ni_3Al(110)$-1Ni, and O/$Ni_3Al(110)$-2Ni surfaces.

The lowest oxygen binding energies for the $Ni_3Al(100)$ surfaces could be for the $Ni_3Al(100)$-1Al or $Ni_3Al(100)$-2Al surface in different situations. Specifically, at the beginning oxygen coverage (0.25 ML), the binding energy of oxygen with the $Ni_3Al(100)$-1Al surface is lower than that of the $Ni_3Al(100)$-2Al surface. At the oxygen coverage of 0.5 ML, the oxygen binding energy for the $Ni_3Al(100)$-2Al surface surpasses that the $Ni_3Al(100)$-1Al surface slightly. With increasing the oxygen coverage to 0.75 ML and then to 1 ML, the binding energy for the $Ni_3Al(100)$-2Al suface becomes the lowest, and the difference in the values of the binding energies of those two surfaces increases. As discussed in section 3.1, the perfect $Ni_3Al(100)$ surface represents the most stable configuration among the clean surfaces with and without antisite defects, while in the process of oxidation the $Ni_3Al(100)$ surfaces with different Al antisite defects become

DOI: 10.1021/acs.jpcc.7b04674
J. Phys. Chem. C 2017, 121, 19191–19200

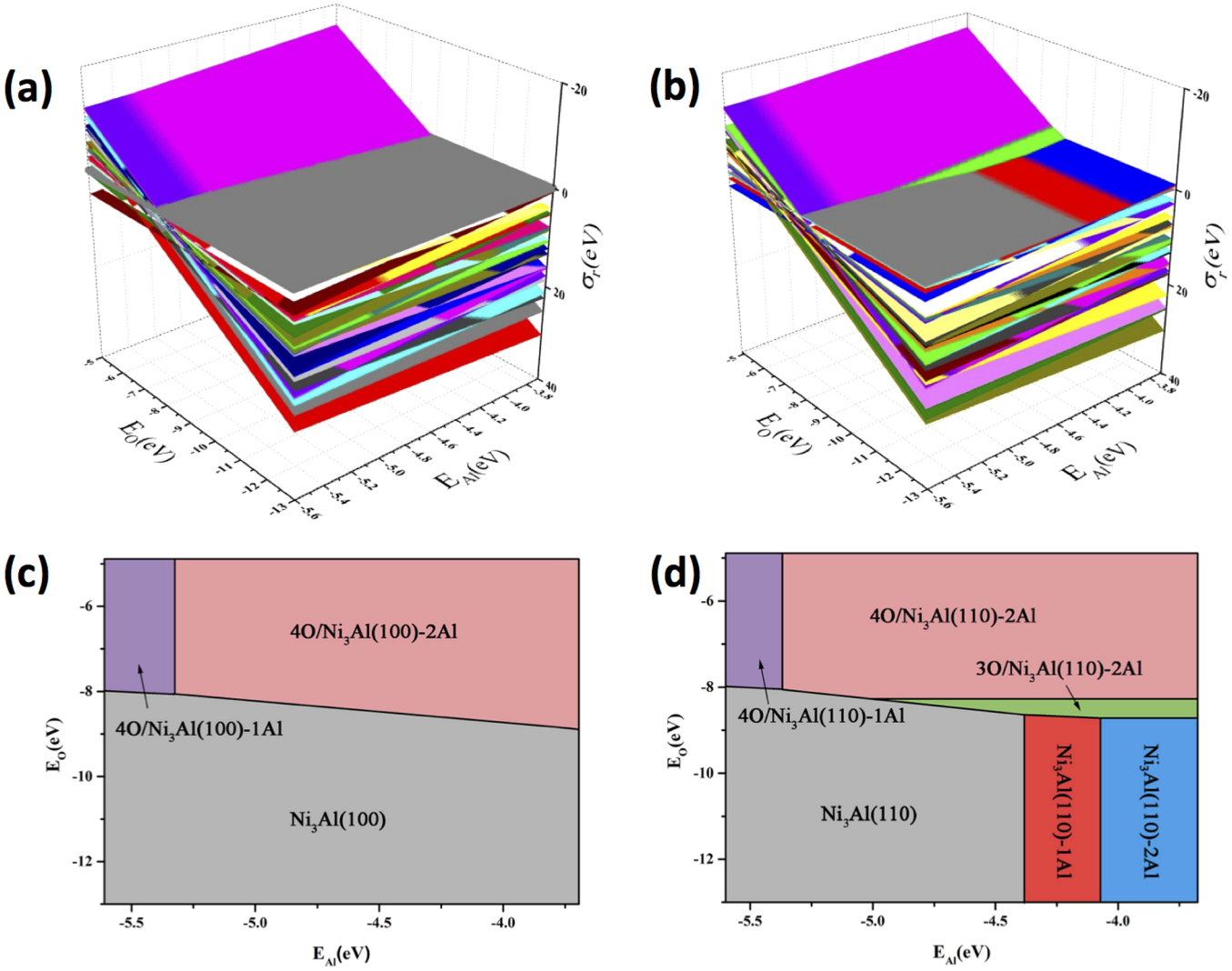

Figure 5. Calculated three-dimensional surface phase diagrams (a, b) and the corresponding two-dimensional surface phase diagrams (c, d) at the different surfaces of $Ni_3Al(100)$ and $Ni_3Al(110)$ as functions of E_{Al} and E_O. Each plane corresponds to one of the tested surface configurations, and only the most stable configurations are considered.

the more stable configuration. The calculation results show that the adsorption of oxygen can enhance the surface segregation of Al, resulting in the formation of the top surface layer with all the Al atoms. For $Ni_3Al(110)$, the oxygen binding energies for the $Ni_3Al(100)$-2Al surface are always the lowest. While the perfect $Ni_3Al(110)$ surface represents the most stable configuration among the clean surfaces over the dominant Al chemical potentials, adsorption of oxygen also enhances the surface segregation of Al, the same as for the $Ni_3Al(100)$ surfaces. Those results are similar to the surface segregation of boron upon hydrogen adsorption on the Si(111)−B surface.[34,35]

3.3. Surface Phase Diagram. In order to further understand the oxidation characteristics of the Ni_3Al surfaces from the thermodynamics point of view, we construct three-dimensional surface phase diagrams of relative surface energies as functions of the chemical potentials of both E_{Al} and E_O for oxygen adsorption on the different $Ni_3Al(100)$ and $Ni_3Al(110)$ surfaces, as shown in parts a and b of Figure 5, respectively. Three dimensional surface diagrams were previously used to elucidate the oxidation mechanism of other similar systems.[36,37] Projecting the lowest surface free energies of the different $Ni_3Al(100)$ and $Ni_3Al(110)$ surfaces in the three-dimensional surface phase diagram onto the two-dimensional plane, we can obtain the corresponding two-dimensional surface phase diagrams, which are shown in parts c and d of Figure 5, respectively.

For the $Ni_3Al(100)$ surface, we can observe that under the O-poor condition, the perfect $Ni_3Al(100)$ is the most stable one. As the oxygen content increases, the 4O/$Ni_3Al(100)$-2Al surface (corresponding to the O coverage of 1 ML) is the most stable configuration, which occupies the most part of the Al chemical potential space. This suggests that O induces the complete Al surface segregation. Note that under the O-rich condition, both 4O/$Ni_3Al(100)$-2Al and 4O/$Ni_3Al(100)$-1Al surfaces can be the most stable configuration, depending on the range of the Al chemical potential. The 4O/$Ni_3Al(100)$-1Al configuration becomes the preferred one when Al is almost oxidized in the area. Since the space occupied by the 4O/$Ni_3Al(100)$-2Al configuration (under the O-rich condition) is much larger than that by the 4O/$Ni_3Al(100)$-1Al configuration, the former is thermodynamically more favorable, implying that all the Al atoms can be totally oxidized during the oxidation process.

DOI: 10.1021/acs.jpcc.7b04674
J. Phys. Chem. C 2017, 121, 19191−19200

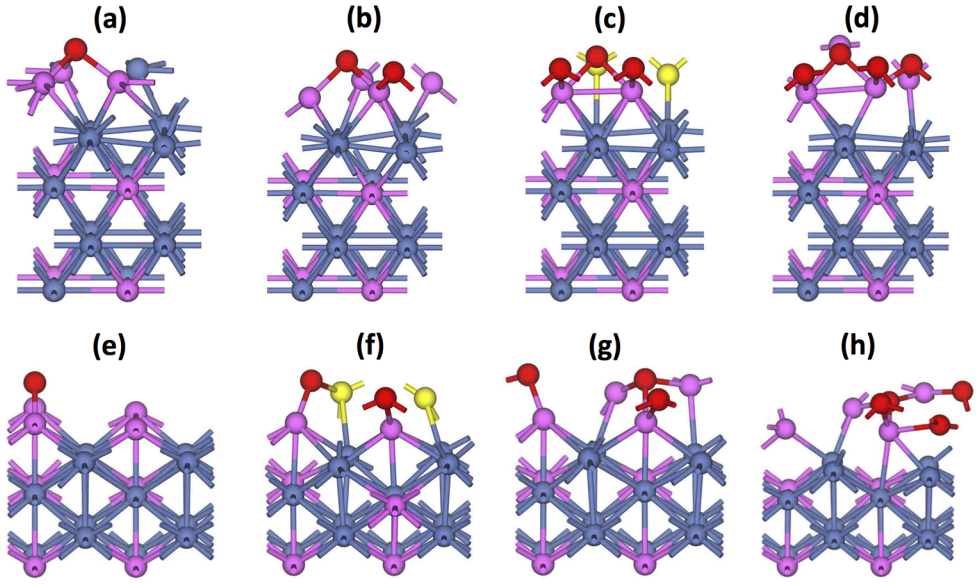

Figure 6. Schematic side views of the atomic structure of 1O/Ni_3Al(100)-1Al (a), 2O/Ni_3Al(100)-2Al (b), 3O/Ni_3Al(100)-2Al (c), and 4O/Ni_3Al(100)-2Al (d), and 1O/Ni_3Al(110)-2Al (e), 2O/Ni_3Al(110)-2Al (f), 3O/Ni_3Al(110)-2Al (g), and 4O/Ni_3Al(110)-2Al (h). Red, blue, and pink/yellow spheres represent O, Ni, and Al atoms, respectively.

Similar to the Ni_3Al(100) surface, the perfect Ni_3Al(110) surface is the lowest under the O-poor and Al-poor conditions. Under the O-poor and Al-rich conditions, Ni_3Al(110)-1Al is the most stable configuration, and at the slightly greater Al chemical potentials, Ni_3Al(110)-2Al is the most stable, indicating that Al segregates to the surface naturally. As the oxygen content increases, we can observe that 3O/Ni_3Al(110)-2Al becomes the most stable configuration under the Al-rich condition, including the area occupied by the Ni_3Al(110)-1Al surface, which means that O promotes the Al segregation from the substrate during the oxidation process. On the O-rich chemical potential space the surface phase diagram is occupied by 4O/Ni_3Al(110)-2Al under the Al-rich condition and by 3O/Ni_3Al(110)-2Al under the Al-poor condition, while the former occupies the far larger area. Under the Al-poor condition, the perfect Ni_3Al(110) is finally oxidized to 4O/Ni_3Al(110)-1Al or 4O/Ni_3Al(110)-2Al; this also proves that O promotes the Al segregation from the substrate.

3.4. Comparison of the Oxidation Process of Ni_3Al-(100) and -(110). As we discuss above, the surface configurations of 1O/Ni_3Al(100)-1Al, 2O/Ni_3Al(100)-2Al, 3O/Ni_3Al(100)-2Al, and 4O/Ni_3Al(100)-2Al have the most negative oxygen binding energies at the different oxygen coverages of 0.25, 0.5, 0.75, and 1 ML, respectively, for oxygen adsorption on the Ni_3Al(100) surface. The surface configurations of 1O/Ni_3Al(110)-2Al, 2O/Ni_3Al(110)-2Al, 3O/Ni_3Al(110)-2Al, and 4O/Ni_3Al(110)-2Al have the most negative oxygen binding energies at the oxygen coverage of 0.25, 0.5, 0.75, and 1 ML, respectively, for oxygen adsorption on the Ni_3Al(110) surface. The atomic structures of those configurations from the side view are displayed in Figure 6a–g.

Figure 6a shows the fully relaxed structure of the 1O/Ni_3Al(100)-1Al configuration with the oxygen coverage of 0.25 ML. At this oxygen coverage, the oxygen atom adsorbs preferentially at the H1 site and bonds with three neighboring Al atoms in a tetrahedral fashion (note that it is not a complete tetrahedron due to the lack of an Al atom at the top corner). The measured Al–O bond lengths and Al–O–Al bond angles of this tetrahedron are 1.87, 1.87, and 1.84 Å and 91.3°, 91.3°, 96.1°, respectively. By contrast, the oxygen adsorption on the Ni_3Al(110) surface occurs preferentially at the B1 site at the coverage of 0.25 ML with the most favorable configuration of 1O/Ni_3Al(110)-2Al. Figure 6e shows the fully relaxed structure with the adsorption of the oxygen atom at the B1 site, where the oxygen atom bonds with two neighboring Al atoms. The adsorption of the first O atom causes the slight lateral relaxation of Al atoms in 1O/Ni_3Al(100)-1Al, while there are no obvious lateral or vertical shifts of the Al atoms in 1O/Ni_3Al(110)-2Al.

For the next oxygen coverage (0.5 ML), the newly absorbed oxygen atom for the (100) surface stays preferentially at the H4 site and the resulting most favorable configuration of 2O/Ni_3Al(100)-2Al is shown in Figure 6b. It is interesting to note that the 2O/Ni_3Al(100)-1Al is not the most favorable configuration. The adsorption of two O atoms also causes the slight lateral relaxation of Al atoms in 2O/Ni_3Al(100)-2Al. For the (110) surface, the newly absorbed surface oxygen atom stays preferentially at the B6 site, and the resulting most favorable configuration of 2O/Ni_3Al(110)-2Al is shown in Figure 6f. It can be noted from Figure 6f that the positions of Al atoms in the fully relaxed structure of 2O/Ni_3Al(110)-2Al change appreciably, in which two of the Al atoms (labeled as yellow atoms in Figure 6f) deviate from their original lateral positions by nearly a quarter of the lattice constant and move upward slightly, and the newly absorbed oxygen atom leads to a minor expansion of the top Al layer by 5.6% compared with the perfect Ni_3Al(110).

At the oxygen coverage of 0.75 ML, the newly adsorbed oxygen on the (100) surface stays preferentially at the B2 site in a tetrahedral fashion. Figure 6c illustrates the fully relaxed structure of the resulting 3O/Ni_3Al(100)-2Al configuration, which shows the lateral displacement of two Al atoms (labeled as yellow atoms in Figure 6c) by nearly a quarter of the lattice constant. More importantly, the oxygen atom that initially resides at H4 moves to B6 after the structure relaxation, resulting in 3.7% upward movement of the top Al layer compared with the perfect Ni_3Al(100). The newly adsorbed oxygen on the (110) surface stays preferentially at the B5 site in the tetrahedral fashion, and Figure 6g shows the fully relaxed

DOI: 10.1021/acs.jpcc.7b04674
J. Phys. Chem. C 2017, 121, 19191–19200

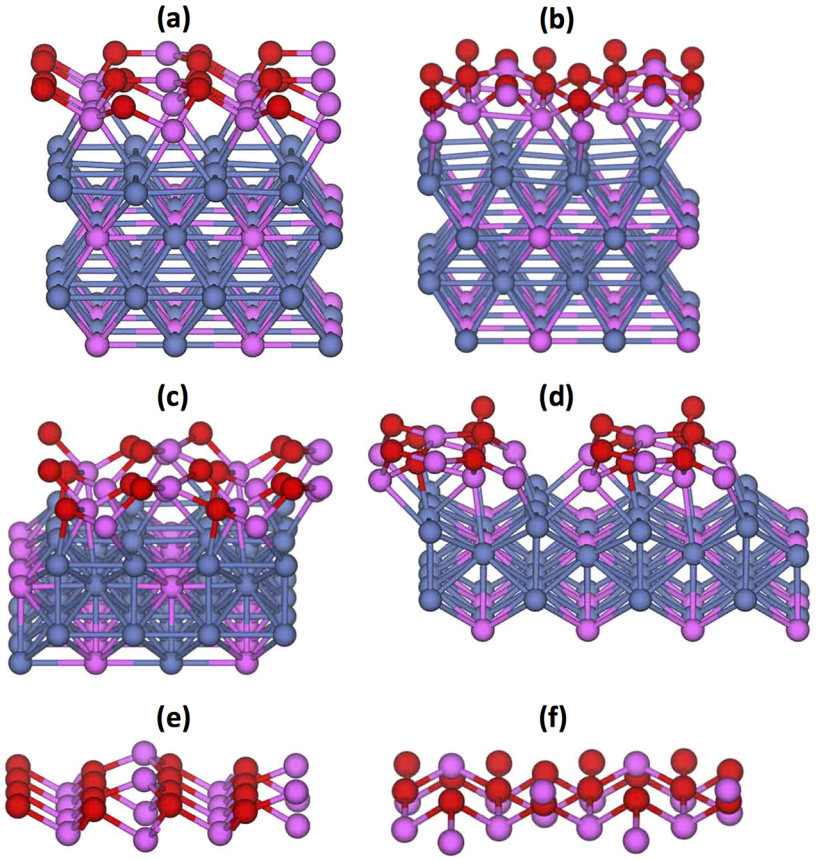

Figure 7. Fully relaxed atomic structure of the 4O/Ni_3Al(100)-2Al (2 × 2) supercell in the [011] (a) and [0$\bar{1}$1] (b) side view, 4O/Ni_3Al(110)-2Al (2 × 2) supercell in the [001] (c) and [1$\bar{1}$0] (d) side view, and γ-Al_2O_3 in the [010] (e) and [100] (f) side view. Red, blue, and pink spheres represent O, Ni, and Al atoms, respectively.

structure of the resulting most favorable 3O/Ni_3Al(110)-2Al configuration. The top Al layer has slight lateral and 7.9% upward displacement compared with the perfect Ni_3Al(110) surface.

At the final oxygen coverage of 1 ML, the newly adsorbed oxygen at the (100) surface stays favorably at the tetrahedral site of H3. Figure 6d shows the fully relaxed structure of the resulting 4O/Ni_3Al(100)-2Al configuration, from which the Al atoms in the top layer are measured to have undergone the upward relaxation by 7.2% compared to the perfect Ni_3Al(100) surface. For the Ni_3Al(110) surface, the newly adsorbed oxygen stays preferentially at the tetrahedral site of H4, and the fully relaxed structure of the most favorable 4O/Ni_3Al(100)-2Al configuration is shown in Figure 6h. The oxygen adsorption at the coverage results in the upward elevation of the Al atoms in the top layer by 11.2% compared to the perfect Ni_3Al(110) surface.

We further compare the atomic structure of the most favorable configurations of the (100) and (110) surfaces at the oxygen coverage of 1 ML with the structure of bulk Al oxide.[38] Figure 7a illustrates the atomic structure of the 4O/Ni_3Al-(100)-2Al surface in the [011] side view, which shows that the Al atoms tend to locate at the separate atomic planes to develop a corrugated surface configuration, while most of the O atoms tend to have a similar surface height. For comparison, Figure 7e illustrates the bulk γ-Al_2O_3 along the [010] side view, which shows that Al atoms locate at alternate atomic layers and O atoms locate at the same atomic plane, similar to the configuration shown in Figure 7a. Figure 7b shows the 4O/Ni_3Al(100)-2Al structure in the [0$\bar{1}$1] side view and the bulk γ-Al_2O_3 along the [100] side view (Figure 7f), and both show similar corrugations in the positions of Al and O atoms. The average Al−O bond length is 1.82 Å in the Al−O tetrahedrons in bulk γ-Al_2O_3, which is also close to the Al−O bond lengths in the 4O/Ni_3Al(100)-2Al configuration (the average Al−O bond lengths of 1.79 Å). The densities of Al and O in bulk γ-Al_2O_3 are 0.1 and 0.15 atom/Å^2, respectively, while the surface densities of Al and O atoms are 0.16 atom/Å^2 for both Al and O in 4O/Ni_3Al(100)-2Al. Compared to bulk γ-Al_2O_3, the 4O/Ni_3Al(100)-2Al configuration has a higher density of oxygen atoms, suggesting that the top surface of Ni_3Al(100) is completely oxidized at this oxygen coverage. The higher density of Al in 4O/Ni_3Al(100)-2Al causes a shorter Al−O bond length compared to that of bulk γ-Al_2O_3.

Figure 7c illustrates the fully relaxed structure of 4O/Ni_3Al(110)-2Al along the [001] side view, which shows that the surface heights of both Al and O atoms vary greatly, different from the structure of the bulk γ-Al_2O_3 (Figure 7e). Figure 7d illustrates the fully relaxed structure of 4O/Ni_3Al(110)-2Al along the [1$\bar{1}$0] side view, which shows that the O and Al atoms do not occupy the entire surface, leaving some open area. The surface densities of both Al and O are 0.11 atom/Å^2 in 4O/Ni_3Al(110)-2Al, which require the incorporation of more oxygen atoms in order to reach the same density of O in bulk γ-Al_2O_3. Therefore, the 1 ML of oxygen coverage is still not sufficient to form a γ-Al_2O_3-like configuration, and more O atoms are required to adsorb into the 4O/Ni_3Al(110)-2Al surface. The average Al−O bond length is 1.84 Å in the Al−O

DOI: 10.1021/acs.jpcc.7b04674
J. Phys. Chem. C 2017, 121, 19191−19200

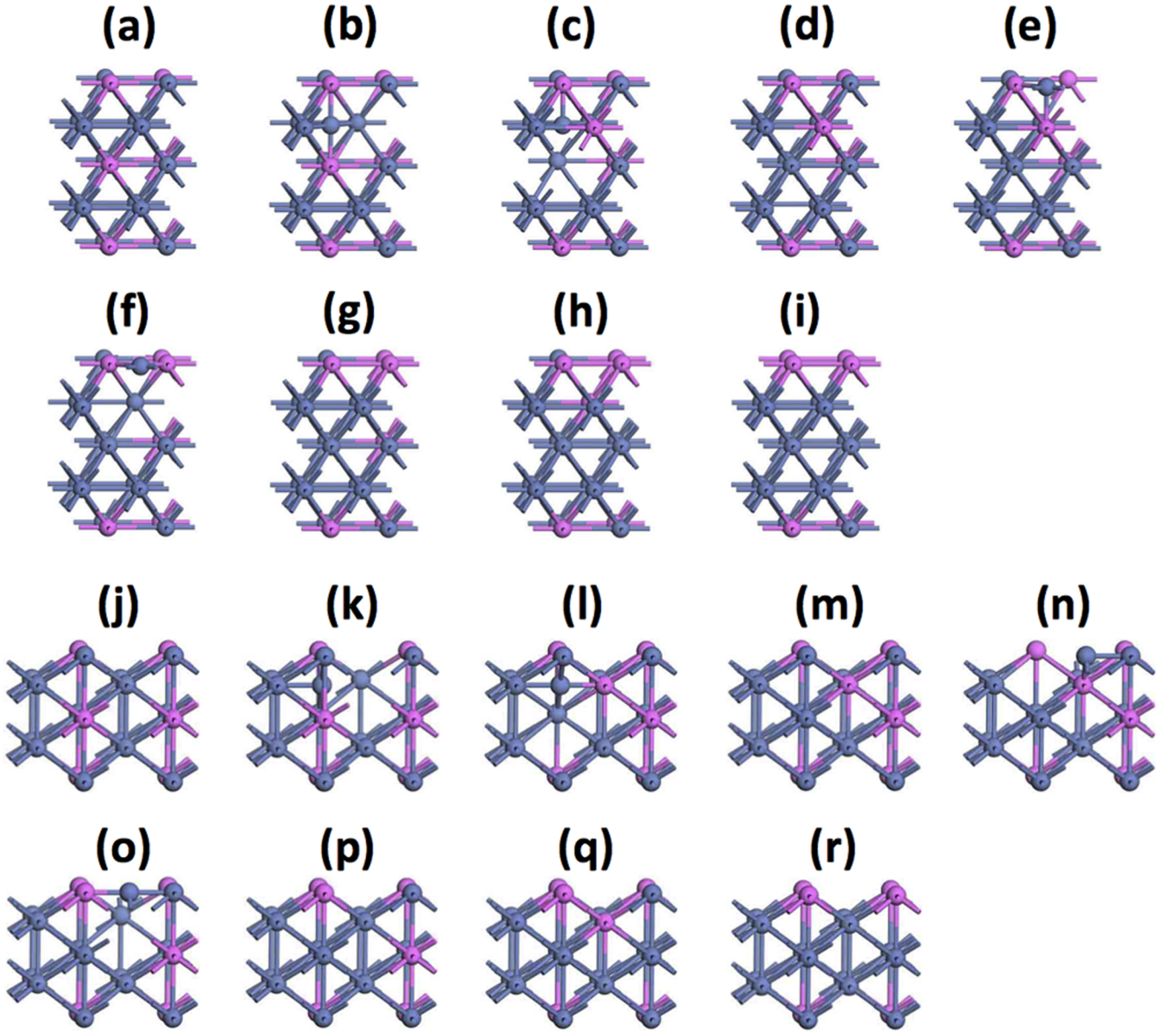

Figure 8. Diffusion pathway of $Ni_3Al(100)$ to develop one surface antisite defect (a–g) and then two surface antisite defects (g–i). Diffusion pathway of $Ni_3Al(110)$ to form one surface antisite defect (j–p) and then two surface antisite defects (p–r). Blue and pink spheres represent Ni and Al atoms, respectively.

tetrahedrons in $4O/Ni_3Al(110)$-2Al and the lower density of O leads to a larger Al–O bond length.

4. DISCUSSION

The DFT results described above show that the perfect surface is the most stable configuration for the $Ni_3Al(100)$ surface, whereas Al antisite defects tend to segregate at the $Ni_3Al(110)$ surface under the nonoxidizing conditions. Such a difference in the two surfaces can be attributed to two reasons. First, the (110) surface has a more open structure than the more densely packed (100) surface, suggesting that the segregation of larger atoms (i.e., Al) to the (110) surface can be more favorable than to the (100) surface (the atomic radii for Ni and Al are 0.124 and 0.143 nm, respectively). In addition, the interlayer spacing for the (110) surface is smaller than that for the (100) surface, which may also facilitate the segregation of Al atoms from the subsurface region to the outer surface.

Our results further show that the oxygen adsorption enhances the Al surface segregation, resulting in the formation of a complete Al surface layer at the initial stage of oxidation for both surfaces. We reach this result by assuming a perfect Ni_3Al supercell slab underneath the surface layer. This can be reasonable if one considers the bulk as an infinite reservoir that can supply Al atoms to the surface layer while causing no changes in composition itself. In reality, however, the oxygen-adsorption-induced formation of Al antisite surface defects requires atom exchanges between the surface and subsurface region. Therefore, the subsurface region is also involved from the beginning of the oxidation process.

As seen in Figure 8a, the formation of Al antisites at the (100) and (110) surfaces requires exchanges of atoms between the topmost and the third layers, because the second layer is pure Ni. Therefore, our calculations involve the migration of Al atoms in the third layer through the second layer and then to

DOI: 10.1021/acs.jpcc.7b04674
J. Phys. Chem. C 2017, 121, 19191–19200

the topmost layer. In this process, an Al atom in the third layer has to exchange the positions, first with a Ni atom in the second layer and then with the Ni atom in the surface layer. Figure 8a–g displays the intermediate snapshots from the NEB-obtained minimum energy reaction path for the formation of an Al antisite on the $Ni_3Al(100)$ surface. Figure 8a shows the perfect $Ni_3Al(100)$ surface without any antisite defects. Figure 8b shows that the atomic exchange can be initiated by the inward migration of the Ni atom in the second layer to an adjacent octahedral interstitial site between the second and third atomic layers (the octahedral site is more favorable than the tetrahedral site because of its larger volume), which results in a vacant site in the second layer. Figure 8c shows the migration of the Al atom in the third layer to the vacant Ni site in second layer, and Figure 8d shows that the dislodged Ni atom in the octahedral site now moves to the vacant Al site in the third layer. In this way, the Al atom in the third layer moves to the second layer by exchanging its site with the Ni atom in the second layer through the interstitial octahedral sites. Similarly, the Al atom in the second layer exchanges with the Ni atom in the first layer through the interstitial octahedral site between the first and second layers, which eventually results in the formation of an Al antisite in the first layer (Figure 8d–g). Figure 8h,i corresponds to the configurations for the formation of the second Al antisite on the (100) surface, which results in a pure Al surface layer. The formation of Al antisite defects on the $Ni_3Al(110)$ surface can occur in the same way through the interstitial octahedral sites, as shown in Figure 8j–r. It is worth mentioning that the presence of point defects in a real sample can significantly facilitate such atom exchanges.

We now consider the effect of oxygen adsorption on the surface segregation of Al atoms. We calculate the system energy by adsorbing four oxygen atoms into each of the intermediate configurations (shown in Figure 8a–r) at the hollow sites of the surface, which corresponds to 1 ML of oxygen coverage, the highest oxygen coverage examined in our study. Figure 9 shows the total energy difference of the intermediate configurations with 1 ML of oxygen coverage. It can be seen that the oxygen adsorption promotes Al segregation for both the (100) and (110) surfaces and such an effect is even stronger for $Ni_3Al(110)$ because the system energy for the $Ni_3Al(110)$ surface is always lower than that for $Ni_3Al(100)$. It can also be noted from Figure 9 that the system energy for the $Ni_3Al(110)$ surface with two Al antisite defects increases dramatically with the oxygen adsorption (such an effect does not show up for the (100) surface). This may be related to the presence of pure Ni layers in the subsurface region of the (110) surface. As shown in Figure 8r, the formation of two Al antisite surface defects results in three pure Ni layers in the subsurface region, which may be highly unfavorable after the oxygen adsorption and likely undergoes further composition evolution by atom exchanges with deeper layers in the bulk. Further investigations to elucidate this composition evolution are needed but are beyond the present study.

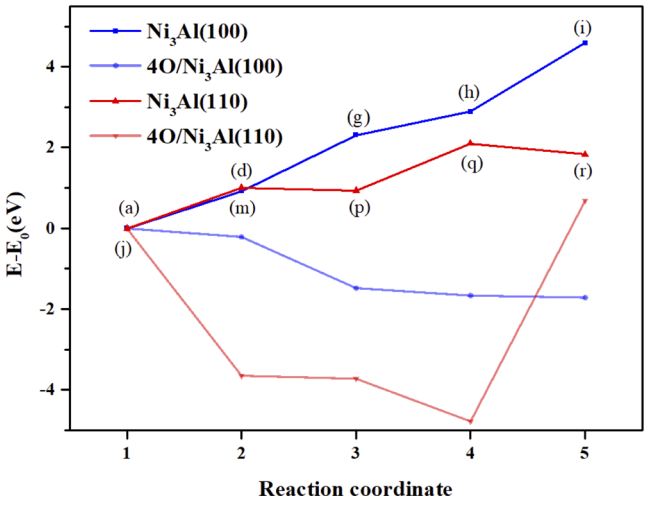

Figure 9. Comparison of the system energies for $Ni_3Al(100)$ and $Ni_3Al(110)$ before and after oxygen adsorption onto the surface of the configurations shown in Figure 8a–r.

5. CONCLUSION

Using the DFT method and thermodynamics calculations, we perform a comparative study of the oxygen adsorption and thermodynamic stabilities of the various $Ni_3Al(100)$ and $Ni_3Al(110)$ surfaces. The relative surface energies of the clean $Ni_3Al(100)$ and $Ni_3Al(110)$ surfaces with different surface antisite defects as functions of the chemical potential of Al are obtained, and we find that the perfect surface is the most stable configuration for the $Ni_3Al(100)$ surface, whereas Al antisite defects tend to segregate at the (110) surface under the nonoxidizing conditions. We have constructed the surface phase diagrams for the $O–Ni_3Al(100)$ and $O–Ni_3Al(110)$ surfaces with different antisite defects under different oxygen coverages. The surface phase diagrams show that the oxygen adsorption enhances the Al surface segregation, resulting in the formation of a complete Al surface layer at the initial stage of oxidation. Compared with the $O–Ni_3Al(100)$ and $O–Ni_3Al(110)$ surfaces, the $Ni_3Al(100)$ surface is thermodynamically more favored to oxidize completely at a lower oxygen coverage.

AUTHOR INFORMATION

Corresponding Authors

*Y.Z. e-mail: zhouyc@xtu.edu.cn.
*G.Z. e-mail: gzhou@binghamton.edu.

ORCID

Guangwen Zhou: 0000-0002-9243-293X

Notes

The authors declare no competing financial interest.

ACKNOWLEDGMENTS

This work was supported by the "Hundred Talents Program" of Hunan Province, China. The work at SUNY Binghamton was supported by the U.S. Department of Energy, Office of Basic Energy Sciences, Division of Materials Sciences and Engineering under Award No. DE-SC0001135.

REFERENCES

(1) Miracle, D. B. The physical and mechanical properties of NiAl. *Acta Metall. Mater.* **1993**, *41*, 649–684.
(2) Davis, J. R. *ASM Specialty Handbook: Nickel, Cobalt, and Their Alloys*; ASM International: Materials Park, OH, 2000.
(3) Finnis, M. W.; Lozovoi, A. Y.; Alavi, A. The oxidation of NiAl: What can we learn from ab Initio calculations? *Annu. Rev. Mater. Res.* **2005**, *35*, 167–207.
(4) Qin, H. L.; Chen, X. D.; Li, L.; Sutter, P. W.; Zhou, G. W. Oxidation-driven surface dynamics on NiAl(100). *Proc. Natl. Acad. Sci. U. S. A.* **2015**, *112*, E103–E109.

DOI: 10.1021/acs.jpcc.7b04674
J. Phys. Chem. C 2017, 121, 19191–19200

(5) Pierce, J. P.; Bartelt, N. C.; Stumpf, R.; McCarty, K. F. Stability of ultrathin alumina layers on NiAl(110). *Phys. Rev. B: Condens. Matter Mater. Phys.* **2008**, *77*, 195438.
(6) Pierce, J. P.; McCarty, K. F. Self-assembly and dynamics of oxide nanorods on NiAl(110). *Phys. Rev. B: Condens. Matter Mater. Phys.* **2005**, *71*, 125428.
(7) Jennison, D. R.; Verdozzi, C.; Schultz, P. A.; Sears, M. P. Ab initio structural predictions for ultrathin aluminum oxide films on metallic substrates. *Phys. Rev. B: Condens. Matter Mater. Phys.* **1999**, *59*, R15605.
(8) Lozovoi, A. Y.; Alavi, A.; Finnis, M. W. Surface energy and the early stages of oxidation of NiAl(110). *Comput. Phys. Commun.* **2001**, *137*, 174−194.
(9) Li, Y. J.; Brndiar, J.; Naitoh, Y.; Sugawara, Y.; Stich, I. Atomic force microscopy identification of Al-sites on ultrathin aluminum oxide film on NiAl(110). *Nanotechnology* **2015**, *26*, 505704.
(10) Liu, S. Y.; Liu, S. Y.; Li, D. J.; Drwenski, T. M.; Xue, W. H.; Dang, H. L.; Wang, S. W. Oxidation mechanism of the intermetallic compound Ti_3Al from ab initio thermodynamics. *Phys. Chem. Chem. Phys.* **2012**, *14*, 11160−11166.
(11) Wagner, C. Theoretical analysis of the diffusion processes determining the oxidation rate of alloys. *J. Electrochem. Soc.* **1952**, *99*, 369−380.
(12) Hohenberg, P.; Kohn, W. Inhomogeneous electron gas. *Phys. Rev.* **1964**, *136*, B864−B871.
(13) Kohn, W.; Sham, L. J. Self-consistent equations including exchange and correlation effects. *Phys. Rev.* **1965**, *140*, A1133.
(14) Kresse, G.; Hafner, J. Ab initiomolecular dynamics for liquid metals. *Phys. Rev. B: Condens. Matter Mater. Phys.* **1993**, *47*, 558−561.
(15) Kresse, G.; Furthmüller, J. Efficient iterative schemes for ab initio total-energy calculations using a plane-wave basis set. *Phys. Rev. B: Condens. Matter Mater. Phys.* **1996**, *54*, 11169−11186.
(16) Kresse, G.; Furthmüller, J. Efficiency of ab-initio total energy calculations for metals and semiconductors using a plane-wave basis set. *Comput. Mater. Sci.* **1996**, *6*, 15−50.
(17) Kresse, G.; Joubert, D. From ultrasoft pseudopotentials to the projector augmented-wave method. *Phys. Rev. B: Condens. Matter Mater. Phys.* **1999**, *59*, 1758−1775.
(18) Blöchl, P. E. Projector augmented-wave method. *Phys. Rev. B: Condens. Matter Mater. Phys.* **1994**, *50*, 17953−17979.
(19) Perdew, J. P.; Chevary, J. A.; Vosko, S. H.; Jackson, K. A.; Pederson, M. R.; Singh, D. J.; Fiolhais, C. Atoms, molecules, solids, and surfaces: Applications of the generalized gradient approximation for exchange and correlation. *Phys. Rev. B: Condens. Matter Mater. Phys.* **1992**, *46*, 6671−6687.
(20) Methfessel, M.; Paxton, A. T. High-precision sampling for Brillouin-zone integration in metals. *Phys. Rev. B: Condens. Matter Mater. Phys.* **1989**, *40*, 3616−3621.
(21) Monkhorst, H. J.; Pack, J. D. Special points for Brillouin-zone integrations. *Phys. Rev. B* **1976**, *13*, 5188−5192.
(22) Rao, P. V. M.; Suryanarayana, S. V.; Murthy, K. S.; Naidu, S. V. N. The high-temperature thermal expansion of Ni_3Al measured by X-ray diffraction and dilation methods. *J. Phys.: Condens. Matter* **1989**, *1*, 5357−5361.
(23) Wu, Q.; Li, S. S.; Ma, Y.; Gong, S. K. Comparison of O adsorption on Ni_3Al (001), (011), and (111) surfaces through first-principles calculations. *Phys. B* **2012**, *407*, 2321−2328.
(24) Kurnosikov, O.; Jurczyszyn, L.; Pieczyrak, B.; Krupski, A. Atomic structure and electronic properties of Ni_3Al(001) surface. *Surf. Sci.* **2008**, *602*, 2994−2999.
(25) Sondericker, D.; Jona, F.; Marcus, P. M. Atomic structure of a {001} surface of Ni_3Al. *Phys. Rev. B: Condens. Matter Mater. Phys.* **1986**, *33*, 900−903.
(26) Sondericker, D.; Jona, F.; Marcus, P. M. Atomic structure of alloy surfaces. III. Ni_3Al{110}. *Phys. Rev. B: Condens. Matter Mater. Phys.* **1986**, *34*, 6775−6778.
(27) Liu, S. Y.; Shang, J. X.; Wang, F. H.; Liu, S. Y.; Zhang, Y.; Xu, H. B. Ab initioatomistic thermodynamics study on the selective oxidation mechanism of the surfaces of intermetallic compounds. *Phys. Rev. B: Condens. Matter Mater. Phys.* **2009**, *80*, 085414.
(28) Piccinin, S.; Stampfl, C.; Scheffler, M. First-principles investigation of Ag-Cu alloy surfaces in an oxidizing environment. *Phys. Rev. B: Condens. Matter Mater. Phys.* **2008**, *77*, 075426.
(29) Qian, G. X.; Martin, R. M.; Chadi, D. J. First-principles study of the atomic reconstructions and energies of Ga- and As-stabilized GaAs(100) surfaces. *Phys. Rev. B: Condens. Matter Mater. Phys.* **1988**, *38*, 7649−7663.
(30) Reuter, K.; Scheffler, M. Composition, structure, and stability of RuO_2(110) as a function of oxygen pressure. *Phys. Rev. B: Condens. Matter Mater. Phys.* **2001**, *65*, 035406.
(31) Liu, S. Y.; Liu, S. Y.; Li, D. J.; Dang, H. l.; Liu, Y. D.; Xue, S.; Xue, W. H.; Wang, S. W. Bonding, stability, and electronic properties of the BC_3 honeycomb monolayer structure on NbB_2(0001). *Phys. Rev. B: Condens. Matter Mater. Phys.* **2013**, *88*, 115434.
(32) Liu, S. Y.; Shang, J. X.; Wang, F. H.; Zhang, Y. Ab initiostudy of surface self-segregation effect on the adsorption of oxygen on the γ-TiAl(111)surface. *Phys. Rev. B: Condens. Matter Mater. Phys.* **2009**, *79*, 075419.
(33) Qin, N.; Liu, S. Y.; Li, Z.; Zhao, H.; Wang, S. First-principles studies for the stability of a graphene-like boron layer on CrB_2(0001) and MoB_2(0001). *J. Phys.: Condens. Matter* **2011**, *23*, 225501.
(34) Wang, S. W.; Radny, M. W.; Smith, P. V. Ab initio cluster calculations of the chemisorption of hydrogen on the Si(111)$\sqrt{3}\times\sqrt{3}$R30°-B surface. *Surf. Sci.* **1997**, *394*, 235−249.
(35) Wang, S. W.; Radny, M. W.; Smith, P. V. Segregation of boron on the cluster-modeled Si(111)$\sqrt{3}\times\sqrt{3}$R30°-B hydrogenated surface. *Phys. Rev. B: Condens. Matter Mater. Phys.* **1997**, *56*, 3575−3578.
(36) Liu, S. Y.; Liu, S.; Li, D. J.; Wang, S.; Guo, J.; Shen, Y. Ab initio atomistic thermodynamics study on the oxidation mechanism of binary and ternary alloy surfaces. *J. Chem. Phys.* **2015**, *142*, 064705.
(37) Liu, S. Y.; Shang, J. X.; Wang, F. H.; Liu, S.; Zhang, Y.; Li, D.; Shields, D.; Xue, W.; Liu, Y.; Dang, H.; Wang, S. Oxidation of the two-phase Nb/Nb_5Si_3 composite: the role of energetics, thermodynamics, segregation, and interfaces. *J. Chem. Phys.* **2013**, *138*, 014708.
(38) Menéndez-Proupin, E.; Gutiérrez, G. Electronic properties of bulk γ−Al_2O_3. *Phys. Rev. B: Condens. Matter Mater. Phys.* **2005**, *72*, 035116.

DOI: 10.1021/acs.jpcc.7b04674
J. Phys. Chem. C 2017, 121, 19191−19200